The accommodation of lithium in bulk ZrO_2

Gareth F. Stephens[1], Yan Ren Than[6], William Neilson[4], Lee J. Evitts[1], Mark R Wenman[3], Samuel T. Murphy[4], Robin W. Grimes[3], Aidan Cole-Baker[2], Susan Ortner[5], Natasha Gotham[5], Michael J. D. Rushton[1], William E. Lee[1,3], Simon C. Middleburgh[1]

[1.] Nuclear Futures Institute, Bangor University, Bangor, LL57 1UT, UK
[2.] Jacobs, Walton House, 404 Faraday Street, Warrington, WA3 6GA, UK
[3.] Department of Materials, Imperial College London, London, SW7 2AB, UK
[4.] Engineering Department, Lancaster University, Lancaster LA1 4YW, UK
[5.] National Nuclear Laboratory, Chadwick House, Warrington WA3 6AE, UK
[6.] Nuclear Research and Safety Initiative, National University of Singapore 138602 – Singapore

Abstract

Lithium is known to accelerate the corrosion of zirconium alloys in light water reactor conditions. Identifying the mechanism by which this occurs will allow alloying additions and alternative coolant chemistries to be proposed with the aim of improved performance. Accommodation mechanisms for Li in bulk ZrO_2 were investigated using density functional theory (DFT). Defects including oxygen and zirconium vacancies along with lithium, zirconium and oxygen interstitials and several small clusters were modelled. Predicted formation energies were used to construct Brouwer diagrams. These show how competing defect species concentrations change across the monoclinic and tetragonal oxide layers. The solubility of Li into ZrO_2 was determined to be very low indicating that Li solution into the bulk, under equilibrium conditions, is an unlikely cause for accelerated corrosion.

1. Introduction

Zirconium alloys are the cladding of choice for the fuel in most pressurised water reactors (PWRs) due to their low thermal neutron capture cross-sections and low corrosion in high temperature, aqueous conditions [1]. Previous publications have shown that zirconium alloy corrosion may occur within a reactor due to gamma and neutron irradiation [2–7]. In the case of radiolysis, this both increases coolant acidity and may also increase the level of oxygen and hydrogen in the coolant, available for the corrosion process [8–10]. Due to boron's high neutron capture cross section, it is often added to the coolant water as a shim against excess reactivity. This addition is in the form of boric acid which further reduces pH necessitating a buffer, which is often in the form of lithium hydroxide [11]. During operation, boron is often found in combination with lithium in thick oxides and CRUD (corrosion products) formed on the cladding, which accumulates in high burnup areas [12]. This is known to cause axial offset anomalies due to the alteration in flux caused by localised high boron concentration. It can reduce reactor efficiency to as low as 70% over several months due to a shutdown margin reduction towards the end of cycle [13,14]. New reactor designs hope to remove the need for boron in favour of a balancing reactivity through control rod movements and burnable absorbers. However, lithium will still be required to mitigate pH changes due to radiolysis [15]. In the absence of boron, lithium has been found to accelerate the corrosion of the

zirconium alloy fuel cladding [6,16–18]. Whilst lithium accelerated corrosion has been demonstrated, the mechanism that underpins this has yet to be identified [19]. The benefits of a better mechanistic understanding cannot be understated as this may lead to innovations for mitigating accelerated corrosion and increasing margins to failure. All of this would increase performance whilst allowing for extended fuel residence times and prolonged, new advanced fuel cycles.

Under normal conditions, zirconium alloy forms two polymorphs of oxide on the surface. For lithium to accelerate corrosion, oxygen must be transported through the zirconium oxide (ZrO_2) layers to the underlying metal substrate. At the oxide/water interface, the monoclinic ZrO_2 polymorph predominates and is known to contain pores that range from 10 to 100 µm in diameter meaning this layer offers little protection [20]. Between the monoclinic oxide layer and the metal substrate is a layer of tetragonal ZrO_2 several hundred nanometres thick [21]. This is the result of the Pilling-Bedworth ratio between the metal substrate and tetragonal oxide layer, where the compressive stresses help stabilize the tetragonal polymorph [22].

This investigation into the bulk monoclinic and tetragonal polymorphs of ZrO_2 probes the impact of lithium at a range of concentrations and identifies subsequent defect concentrations throughout the oxide layers. Brouwer diagrams are created to highlight defect concentrations and are compared to previous investigations [23]. In addition, the solubility of lithium is calculated. These data aid in the development a mechanistic understanding for oxygen transport through the bulk versus other potential routes.

2. Methodology

2.1 Density Functional Theory

Density functional theory (DFT) calculations were undertaken using the Vienna Ab initio Simulation Package (VASP). The Project Augmented Wave pseudopotential library within VASP was utilized with plane wave simulations [24]. A quasi-Newton algorithm was used to relax ions into their instantaneous ground state. In addition, a PBE functional (Perdew-Burke-Ernzerhof) was used with a cut-off energy at 500 eV. Initially a 2×2×2 *k*-point mesh was employed, later increased to a 4×4×4 *k*-point mesh to increase accuracy for all calculations. The electronic relaxation and atomic force threshold criteria were 10^{-4} eV and 10^{-3} eV/Å, respectively. The monoclinic [25] and tetragonal [26] ZrO_2 unit cells containing 4 and 2 formula units, respectively, were first allowed to relax under constant pressure so all cell parameters and atomic positions were optimised. The relaxed unit cells were then extended to a 2×2×2 supercell for the monoclinic ZrO_2 structure containing 32 formula units and a 3×3×2 tetragonal ZrO_2 supercell containing 36 formula units. The dimensions of these supercells were such that each simulation cell had similar dimensions along its three cell vectors. Constant pressure calculations were conducted on the supercells before performing constant volume calculations with the introduction of defects to the supercells to gain final values for further investigations. Constant volume calculations are preformed to restrict zirconium exchange but allow oxygen exchange to/from a hypothetical reservoir [27].

2.2 Brouwer Diagrams

A Brouwer diagram shows defect equilibria for an oxide system by plotting defect concentrations against the partial pressure of oxygen (See section 2.3). In Kröger-Vink notation where × has a neutral charge, • is positive and ′ is negative [28], the defects under consideration were point defects including; $(O_i^{\times})$ (O_i') (O_i''), $(V_O^{\times})$ $(V_O^{\bullet})$ $(V_O^{\bullet\bullet})$, $(Zr_i^{\times})$ $(Zr_i^{\bullet})$ $(Zr_i^{\bullet\bullet})$ $(Zr_i^{\bullet\bullet\bullet})$ $(Zr_i^{\bullet\bullet\bullet\bullet})$, $(V_{Zr}^{\times})$ (V_{Zr}') (V_{Zr}'') (V_{Zr}''') (V_{Zr}''''), $(Li_i^{\times})$ $(Li_i^{\bullet})$ with the addition of a split oxygen interstitial $(O_i^{\times} - Split)$. The split oxygen interstitial contains a displaced oxygen atom and an interstitial oxygen atom equidistant from the original, now vacant, oxygen site (the point defect fractional coordinates may be found in the supplementary material). In addition, small clusters were also considered including {V_O:V_{Zr}}, {V_O:2V_{Zr}}, {Li_i:V_O}, {Li_i:V_{Zr}} and {2Li_i:V_{Zr}} with charges ranging from neutral to ±4 depending on the specific cluster. By calculating the total energies of the perfect structure and structures containing lithium defects, the defect ingress through solubility could also be identified [29] along with formation energy of ionic defects.

DFT can also provide electronic information concerning the perfect supercell structures including band gap, valence and conduction bands, which are used in the creation of the Brouwer diagram, using Fermi-Dirac statistics to provide electron and hole concentrations upon which charge defect equilibria could be attributed. A novel aspect of the Defect Analysis Package V2.7 script created by Murphy and Neilson [30] is that a particular defect concentration may be stipulated where all other defect equilibria, including those of electrons and holes, are calculated. In the case of this investigation, lithium concentrations are stipulated from 10^{-3} to 10^{-11} per ZrO_2 formula unit and a temperature of 635K was used for all calculations as a normal (water) operating temperature of a PWR [31]. In order to account for coulombic self-interaction, the screened Madelung correction was used [32] and the oxygen chemical potential temperature dependence employed the real gas model [33] with the Kasamatsu method used for defect concentration statistics [34]. Further details on Brouwer diagram calculations may be found in recently published work by Neilson *et al.* [35].

2.3. Partial Pressure

Here we use Brouwer diagrams to understand the corrosion behaviour of Zr metal whilst in thermodynamic contact with a source term of lithium ions that represents the lithiated coolant environment. Thus, defect concentrations are plotted against the oxygen partial pressure (P_{O_2}). For simplicity, we consider the highest oxygen partial pressure to be at the coolant-oxide interface. From this interface to the metal-oxide interface, the partial pressure will reduce. Henry's law is used to compute the partial pressure of oxygen (P_{O_2}), , which states that the amount of absorbed oxygen in a liquid is proportional to the partial pressure at the surface. The partial pressure of oxygen, P_{O_2}, at the water-oxide interface will change with temperature and therefore alter the availability of soluble oxygen. However, the proportionality factor in Henry's law is typically measured at room temperature and rarely extended above 100°C [36,37]. However, Tromans [38] deduced a temperature-dependent relationship between the molar solubility, c_{aq}, and partial pressure with:

$$\frac{1}{P_{O_2}} = \frac{\exp\left\{\frac{0.046 \cdot T^2 + 203.35 \cdot T \cdot \ln(T/298) - (299.378 + 0.092 \cdot T)(T - 298) - 20591}{8.3144 \cdot T}\right\}}{c_{aq}} \quad (1)$$

Equation 1 agrees with experiment from room temperature to 616 K [38] with a value of 3.13 x 10^{-8} mol/L molar solubility of oxygen in water; the relationship is illustrated in Figure 1.

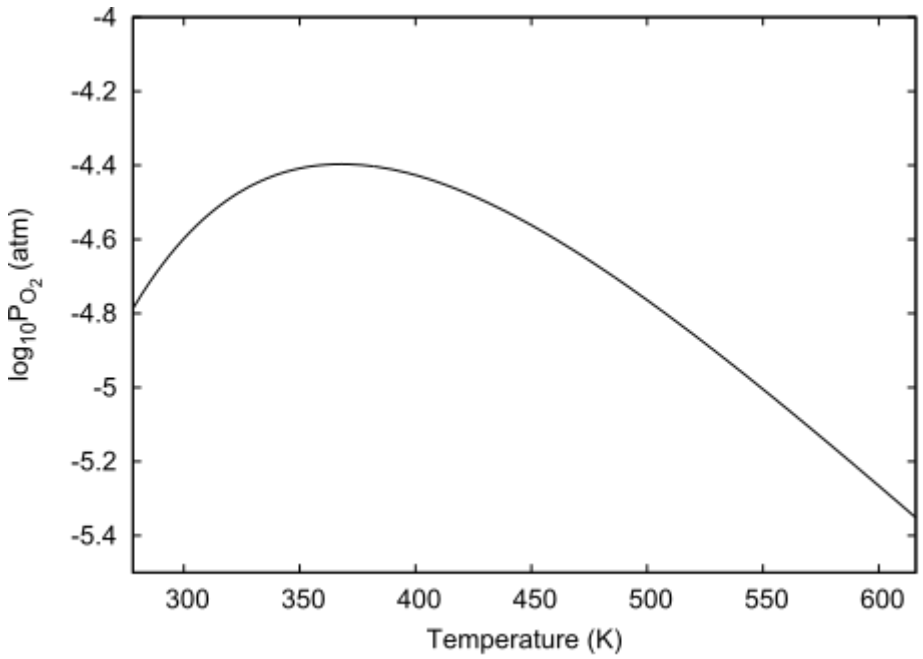

Figure 1: The partial pressure of oxygen in water, between room temperature and 616 K, plotted using Equation 1.

At a temperature of 342°C (616 K) the corresponding partial pressure is -5.35 atm, as seen in Figure 1, and calculating past this to 635 K indicates the partial pressure of oxygen is -5.46 atm, which may be considered as the water/oxide interface position in the Brouwer diagrams presented here. Whilst radiolysis may affect the value of P_{O_2} at the water/oxide interface and into the oxide layers (a likely increase of oxygen availability), this is beyond the scope of the current investigation.

3. Results & Discussion

3.1. Formation energy and Band gap

To identify the dominant charged defect amongst competing defects (i.e., which will exhibit the greatest concentration), all individual defect formation energies must be calculated. A lower formation energy increases the likelihood that the particular charged species will have a higher concentration. The formation energies, however, are plotted against the band gap, up to 3.5 eV for monoclinic and up to 3.8 eV for tetragonal [39], where more negatively charged defects will have a higher concentration at the top part of the band gap (conduction band) and positively charged defects will have higher concentrations at the bottom of the

band gap (valence band). The predicted charge state for a given defect species is established across the band gap by calculating the formation energy, $E^{f}_{X^{q}}$, via:

$$E^{f}_{X^{q}} = E^{DFT}_{X^{q}_{Zr}} - E^{DFT}_{perfect} + \sum_{i} n_i \mu_i + q(E_{VBM} + \mu_e) + E_{SM} \qquad (2)$$

where $E^{DFT}_{perfect}$ is the DFT energy of the perfect cell, $E^{DFT}_{X^{q}_{Zr}}$ is the DFT energy of the defect cell, E_{VBM} is the valence-band maximum of the perfect supercell, n_i is the number of atoms added or removed, and E_{SM} is a charge correction term for the *Screened Madelung* correction for electrostatic self-interaction [32,40]. The parameters μ_i and μ_e are the chemical potentials of the defect species and the electrons relative to E_{VBM}, respectively. The formation energies are plotted against the band gap in Figures 2 and 3, for both the monoclinic and tetragonal forms of ZrO_2, respectively. This methodology has been employed successfully in previous work by Murphy *et al.* [41].

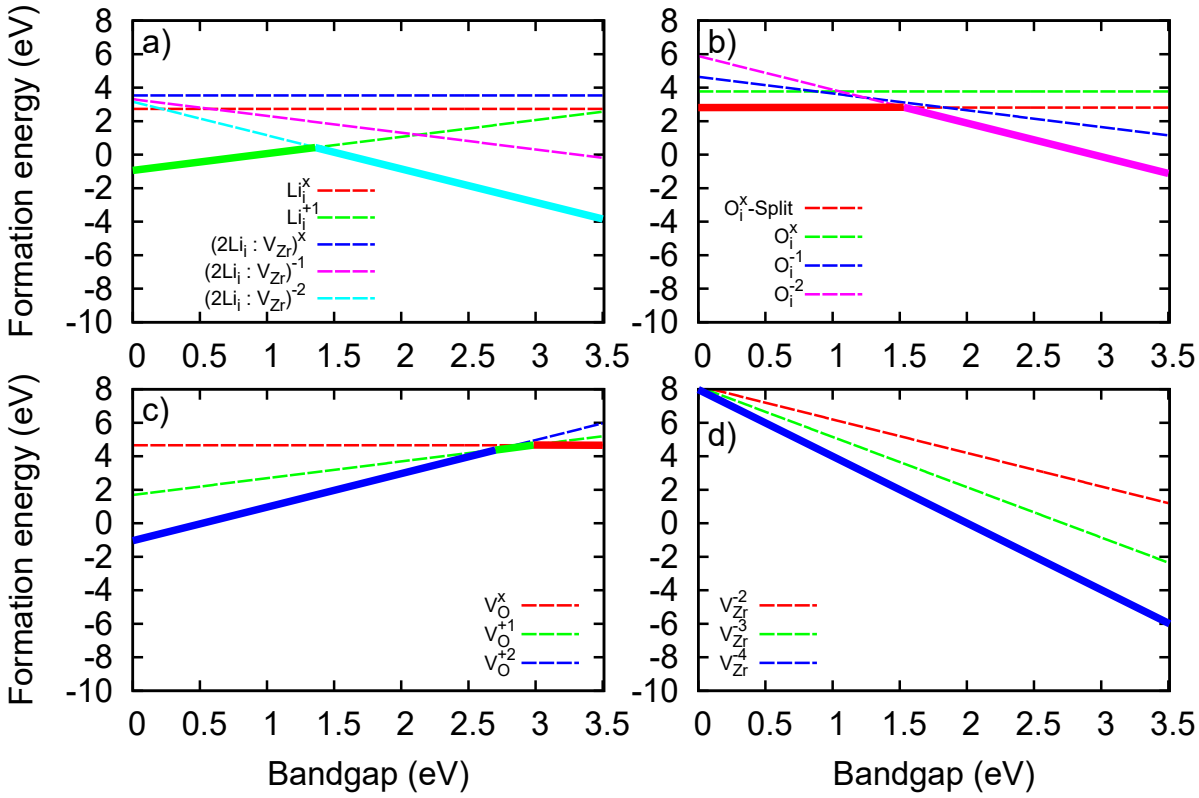

Figure 2. Formation energies for monoclinic ZrO_2 as a function of the Fermi energy for a) lithium defects b) oxygen interstitials c) vacant oxygen d) vacant zirconium. The solid line represents the formation energy minimum for the defect type.

As shown in Figure 2a for lithium defects, singly charged lithium interstitials $(Li_i^{\bullet})$ are dominant from 0 to ~1.4 eV towards the valence band after which the cluster$\{2Li_i^{\bullet}: V_{Zr}^{''''}\}''$ is favoured up to the conduction band at 3.5 eV. In Figure 2b for oxygen interstitials, the neutral charged split interstitial $(O_i^{\times} - split)$ is prevalent in the valence region and the simple doubly charge oxygen interstitial (O_i'') is favoured towards the conduction region. In Figure 2c,

doubly charged oxygen vacancies ($V_O^{\bullet\bullet}$) are prevalent across most of the band gap from the valence band through to ~2.8 eV with the remaining being neutral vacancies ($V_O^{\times}$) at the conduction band. Finally, in Figure 2d, the fully charged zirconium vacancy (V_{Zr}'''') is dominant throughout the band gap. Similar results are observed for tetragonal ZrO_2 as illustrated in Figure 3 .

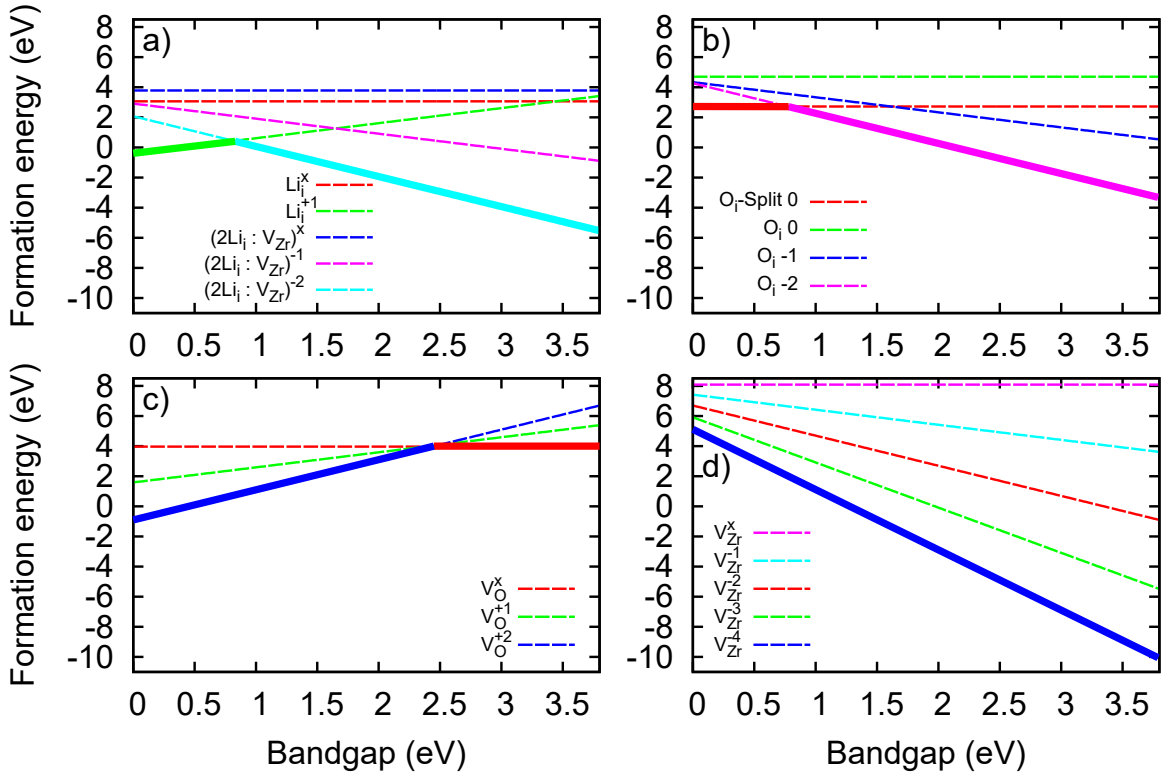

Figure 3. Formation energies for tetragonal ZrO_2 as a function of the Fermi energy for a) lithium defects b) oxygen interstitials c) vacant oxygen d) vacant zirconium. The solid line represents the formation energy minimum for the defect type.

3.2. Brouwer Diagrams

Brouwer diagrams for the monoclinic and tetragonal ZrO_2 polymorphs at constant volume are plotted in Figures 4 and 5, respectively. The plots show the log of defect concentrations against the log of partial oxygen pressure. Lithium has a constant concentration throughout the partial pressure range, and charge neutrality is conserved throughout, and includes electrons, holes and defects. The range of defect concentrations were limited to 10^{-20} per ZrO_2 as defect concentrations below this level were considered negligible. The water/oxide interface is marked at the higher partial pressure with a reducing partial pressure moving left towards the metal/oxide interface.

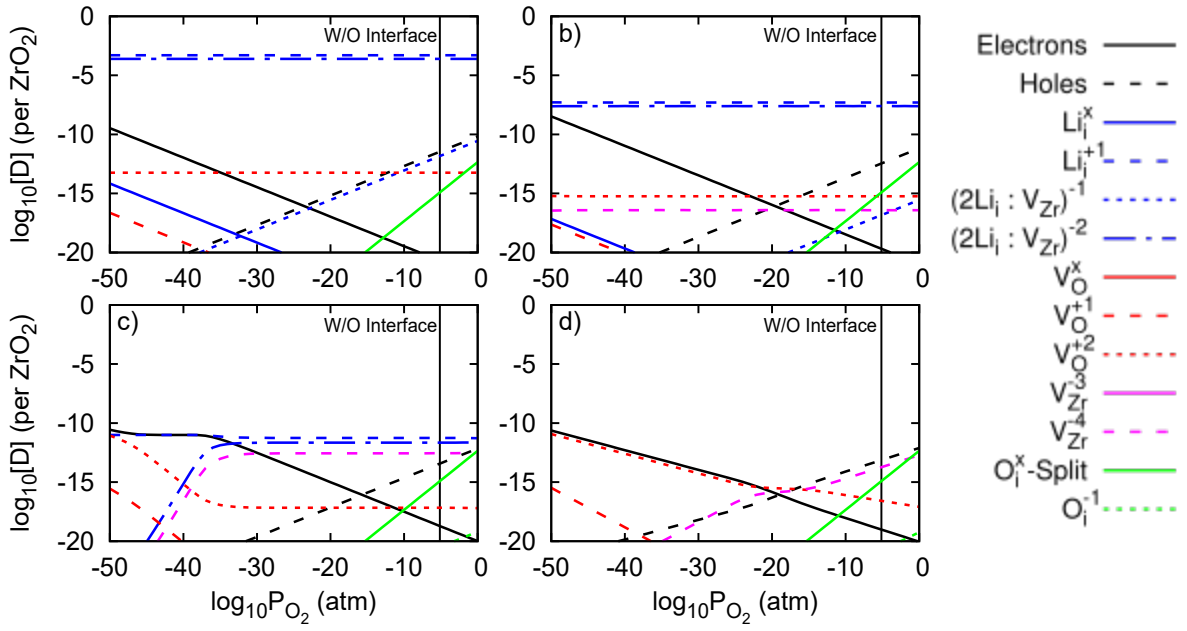

Figure 4: Brouwer diagrams at 635 K showing defect concentrations [D] per unit monoclinic ZrO_2 for (a) 10^{-3} Li per ZrO_2 (b) 10^{-7} Li per ZrO_2 (c) 10^{-11} Li per ZrO_2 and (d) no lithium concentration. The faint vertical black line represents the water oxide interface.

When considering a comparison with previously published Brouwer diagrams, the non-lithiated Figure 4d confirms past attempts that used Boltzmann statistics with only subtle differences where electron and hole concentrations were equal for a short range of partial pressure at the point of intercept [23]. However, here we show Fermi-Dirac statistics which highlight a single point convergence and divergence of electrons and holes. With further comparison of the previously published work of the diagram without lithium, defects follow the same trend where double charged vacant oxygen ($V_O^{\bullet\bullet}$) and electrons dominate low P_{O_2} and zirconium vacancies ($V_{Zr}^{''''}$) along with holes are dominant towards the oxide/water interface at higher P_{O_2}.

As lithium is added to the monoclinic system at concentrations of 10^{-11} per ZrO_2 (Figure 4c), ($V_O^{\bullet\bullet}$) and ($V_{Zr}^{''''}$) concentrations remain the same at log P_{O_2}= 0, however, as partial pressure is reduced moving into the material, ($V_{Zr}^{''''}$) concentrations increase relative to the undoped system, whilst ($V_O^{\bullet\bullet}$) decreases. Additionally, electron concentrations are equal to the concentration of lithium at very low partial pressures.

Considering the concentration of 10^{-3} lithium per ZrO_2 formula unit, the dominant lithium defects are ($Li_i^{\bullet}$) and the $\{2Li_i^{\bullet}:V_{Zr}^{''''}\}''$ cluster, which share similar concentrations across the PO2 range modelled. The same observation holds true when the total lithium concentration is reduced to 10^{-7}. At higher lithium concentrations, the electron concentration is slightly higher at lower P_{O_2}. However, as the lithium concentrations become comparable to that of electrons at 10^{-11} Li concentration, the ($Li_i^{\bullet}$) and electrons are charged balanced causing an increase of electron concentration at low P_{O_2}. Conversely, the $\{2Li_i^{\bullet}:V_{Zr}^{''''}\}''$ cluster is charge balanced by ($V_{Zr}^{''''}$) causing a reduction of $\{2Li_i^{\bullet}:V_{Zr}^{''''}\}''$ concentration at lower P_{O_2}. The relationship between $\{2Li_i^{\bullet}:V_{Zr}^{''''}\}''$ and ($V_O^{\bullet\bullet}$) can be seen where at 10^{-3} and 10^{-7} lithium

concentration, the ($V_O^{\bullet\bullet}$) shows a linear relationship on the graph between lithium and oxygen vacancies. As the $\{2Li_i^{\bullet}:V_{Zr}^{''''}\}''$ concentration drops, due to electron and ($V_{Zr}^{''''}$) concentrations at 10^{-11} Li concentration, the ($V_O^{\bullet\bullet}$) is facilitated to increase in concentration at low P_{O_2}.

As lithium concentrations are increased to 10^{-7} (Figure 4b) and then further up to 10^{-3} (Figure 4a), the isolated zirconium vacancy ($V_{Zr}^{''''}$) reduces as the $\{2Li_i^{\bullet}:V_{Zr}^{''''}\}''$ concentration increases (where the vacancy is bound within the structure). Oxygen vacancy ($V_O^{\bullet\bullet}$) concentrations show a linear increase with Li concentration, although their concentration remains lower than the concentrations necessary to impact significant changes in bulk behaviour. There are negligible changes in concentration for ($V_O^{\bullet}$) defects at extremely low partial pressures and split oxygen interstitial at the high partial pressures. A bond length of 1.49 Å for the split interstitial was observed, consistent with a peroxide ion defect that has been previously observed in MgO [42], ThO_2, amorphous ZrO_2 [43] and yttria doped zirconia [5].

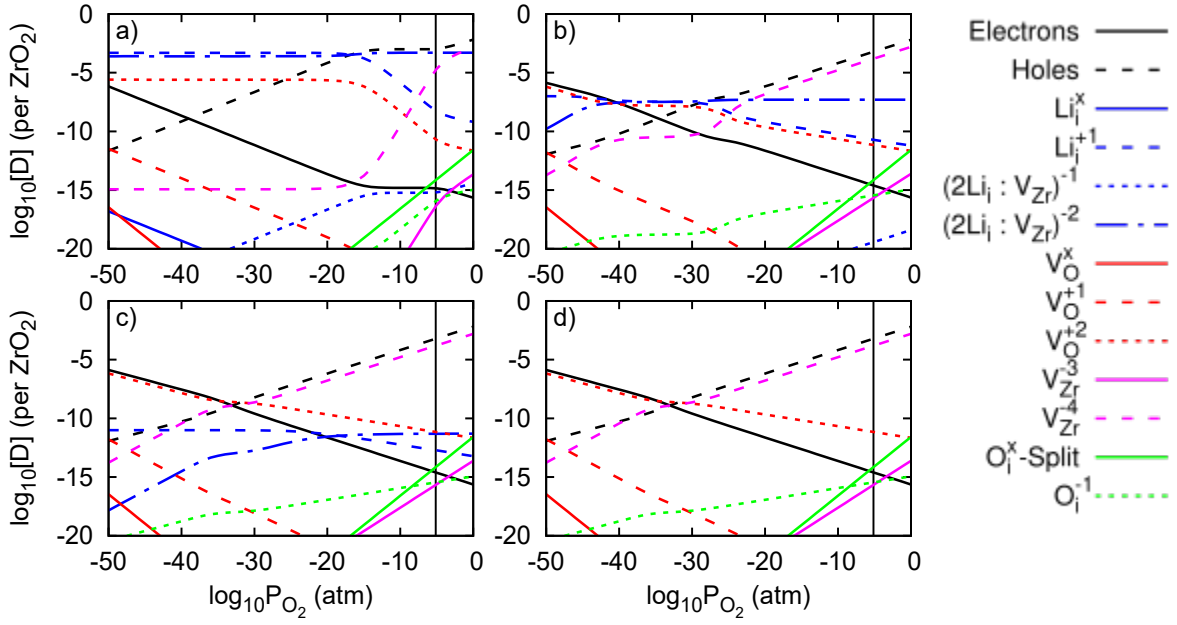

Figure 5: Brouwer diagrams at 635 K showing defect concentrations [D] per unit tetragonal ZrO_2 for (a) 10^{-3} Li per ZrO_2 (b) 10^{-7} Li per ZrO_2 (c) 10^{-11} Li per ZrO_2 and (d) no lithium concentration. The faint vertical black line represents the water oxide interface.

In Figure 5, it is apparent that the overall defect concentrations for the tetragonal polymorph are higher than in the monoclinic case. Comparing the undoped cases in Figure 4d and 5d, the increased concentration of defects in the tetragonal system suggests an increase in overall corrosion limiting defect carriers, highlighting the lack of protection afforded by the tetragonal layer in this regard. In addition, the intersection of the curves for electrons and holes occurs at lower partial pressures corresponding to a position further into the oxide away from the coolant interface.

Where the monoclinic polymorph shows ($V_{Zr}^{''''}$) concentrations that are below 10^{-20} concentration at high lithium concentrations, 10^{-3}, the ($V_{Zr}^{''''}$) and ($V_O^{\bullet\bullet}$) maintain

concentrations at zero log partial pressure regardless of lithium concentrations in the tetragonal structure. It is also observed that the point of intersection between ($V_{Zr}^{''''}$) and ($V_O^{\bullet\bullet}$) is brought closer to the surface with an increase of lithium.

At the highest lithium concentration, ($V_O^{\bullet\bullet}$) is dominant for most of the partial pressure range only to be overtaken by ($V_{Zr}^{''''}$) near to the surface. As with the monoclinic polymorph, the lithium is predominantly accommodated through lithium interstitials of +1 charge and a small cluster of two lithium atoms around a vacant zirconium site with an effective -2 charge. Due to the overall higher defect concentrations for the tetragonal polymorph, at Li concentrations of 10^{-11} per ZrO_2 and less, there is little change when compared to the lithium free Brouwer diagram. As with the monoclinic polymorph, the dominant lithium defects are ($Li_i^{\bullet}$) and the $\{2Li_i^{\bullet}:V_{Zr}^{''''}\}''$ cluster. However, close to the water oxide interface at higher P_{O_2}, the ($Li_i^{\bullet}$) is reduced in concentration due to an increase of holes. This interaction allows for an increase of ($V_O^{\bullet\bullet}$) and a reduction of ($V_{Zr}^{''''}$) close to the water oxide interface. As the lithium concentrations drop to 10^{-11} and below, the lithium no longer has an impact on electron, hole, oxygen or zirconium defects. Previous Brouwer diagram literature shows the tetragonal polymorph at temperatures ranging up to 1500 K [32,44]. The higher temperatures, which are well above expected operational temperature, may account for additional stress of the tetragonal polymorph. However, here, the overall picture remains the same as can be seen in Figure 5 and, as such, the higher temperatures have been omitted.

3.4. Predicting the Solubility of Li in Bulk ZrO_2

The equilibrium solubility of Li into bulk ZrO_2 can be predicted by reviewing the results of the Brouwer diagrams, Figures 4 and 5, forming reactant and product equations that can be used in conjunction with DFT values to predict solution energies. In all cases the reference state is chosen to be the ternary Li_2ZrO_3. Higher solution energies are associated with lower lithium concentration and vice versa. For completeness, the values for both monoclinic and tetragonal solution energies are provided for each reaction.

According to the Brouwer diagrams, at high oxygen partial pressures ,Li is accommodated via charged lithium-zirconium vacancy clusters ($\{2Li_i^{\bullet}:V_{Zr}^{''''}\}''$) that are charge balanced with ($Li_i^{\bullet}$) that can be described via the following reaction from Li_2ZrO_3:

$$2Li_2ZrO_3 + \frac{1}{2}O_2 + Zr_{Zr}^{\times} \rightarrow \{2Li_i^{\bullet}:V_{Zr}^{''''}\}'' + 2Li_i^{\bullet} + 2ZrO_2 \quad (3)$$

The reaction energies are large: 4.06 eV per Li for monoclinic and 5.8 eV for the tetragonal zirconia. These values are consistent with Li exhibiting an extremely low solubility at higher oxygen partial pressures.

At lower oxygen partial pressures, Figures 4a and 5a indicate oxygen vacancies ($V_O^{\bullet\bullet}$) charge balance the ($\{2Li_i^{\bullet}:V_{Zr}^{''''}\}''$) cluster and ($Li_i^{\bullet}$). When considering the vacant oxygen charge balance to the cluster, the following solution reaction can be considered from Li_2ZrO_3:

$$Li_2ZrO_3 + O_O^{\times} + Zr_{Zr}^{\times} \rightarrow \{2Li_i^{\bullet}:V_{Zr}^{''''}\}'' + V_O^{\bullet\bullet} + 2ZrO_2 \quad (4)$$

The predicted solution energies are 8.58 eV per Li into tetragonal and 5.34 eV into monoclinic ZrO_2. Again, solution energies are high indicating that Li bulk solubility will be very limited.

4. Summary

The defect formation energies presented in figures 2 and 3 indicate which charges are preferred across the band gaps, with ($V_O^{\bullet\bullet}$) being dominant at the valence band and ($V_{Zr}^{''''}$) at the conduction band. For lithium defects, the ($\{2Li_i^{\bullet}:V_{Zr}^{''''}\}''$) cluster is dominant for most of the band gap with a small preference for ($Li_i^{\bullet}$) at the valence band end. This means, when positioned on the Brouwer diagram, high electron concentrations will favour the positive ($Li_i^{\bullet}$), and higher hole concentrations will favour the ($\{2Li_i^{\bullet}:V_{Zr}^{''''}\}''$).

The Brouwer diagrams presented in this investigation that used Fermi-Dirac statistics gave subtle differences, with enhanced accuracy but do not fundamentally alter the picture previously reported in literature when considering no lithium [23]. The ability to stipulate a defect species concentration is novel to the Brouwer diagram script created by Murphy *et al.* [30]. This is particularly advantageous as it provides a basis for comparison in real world applications where lithium concentrations are added to coolant water within a nuclear reactor. Should lithium have entered into solid solution, the Brouwer diagrams would offer insight into the implications for altered defect concentrations that may aid in the transport of oxygen to the metal substrate, effectively enhancing corrosion rates. The Brouwer diagrams indicate that the oxygen vacancy concentration is increased by the presence of lithium. It has been previously reported that lithium, ($Li_i^{\bullet}$), can reduce the volume of both monoclinic and the tetragonal polymorphs [23]. By combining the volume changes from all defect concentrations included in the Brouwer diagrams with constant pressure calculations that allow for volumetric relaxation, a small reduction in volume for the monoclinic polymorph was observed with a minimal effect to the tetragonal polymorph. However, due to the very low predicted lithium bulk solubility, this may be largely discounted.

To conclude, due to the high predicted solution energies of lithium into bulk ZrO_2 polymorphs, it is reasonable to discount the idea that lithium accelerated corrosion proceeds via modification of the bulk oxide. This is consistent with current literature, which indicates lithium segregates along grain boundaries rather than via bulk ingress [45]. Grain boundary effects could facilitate oxygen transport where surface effects could facilitate the dissociation of water or a potential drop across the oxide. Future work will use the methods developed here to consider amorphous structures to provide an insight into grain boundary defect behaviour.

Acknowledgments

GFS is supported by Jacobs and the ESPRC through the Nuclear Energy Futures Centre for Doctoral Training (CDT - EP/S023844/1). The project is part of the Westinghouse led MUZIC-3 research programme and MIDAS project (EP/S01702X/1). We would like to thank Supercomputing Wales for provision of computational resources. SCM, WEL and MJDR are funded through the Sêr Cymru II programme by Welsh European Funding Office (WEFO) under the European Development Fund (ERDF). Computing resources were made available by HPC Wales and Supercomputing Wales. STM and WN acknowledge funding from EPSRCs

TRANSCEND project (EP/S01019X/1). Structures were obtained with the use of the EPSRC funded Physical Sciences Data-science Service hosted by the University of Southampton and STFC under grant number EP/S020357/1.

References

[1] L. Hallstadius, S. Johnson, E. Lahoda, Cladding for high performance fuel, Prog. Nucl. Energy. 57 (2012) 71–76. https://doi.org/10.1016/j.pnucene.2011.10.008.

[2] B. Cox, Is zirconium oxide morphology on fuel cladding largely determined by lithium hydroxide concentration effects?, J. Nucl. Mater. (1997). https://doi.org/10.1016/S0022-3115(97)00192-X.

[3] J. Yang, M. Youssef, B. Yildiz, Oxygen self-diffusion mechanisms in monoclinic ZrO_2 revealed and quantified by density functional theory, random walk analysis, and kinetic Monte Carlo calculations, Phys. Rev. B. 97 (2018). https://doi.org/10.1103/PhysRevB.97.024114.

[4] K. Annand, M. Nord, I. MacLaren, M. Gass, The corrosion of $Zr(Fe, Cr)_2$ and Zr_2Fe secondary phase particles in Zircaloy-4 under 350 °C pressurised water conditions, Corros. Sci. 128 (2017) 213–223. https://doi.org/10.1016/j.corsci.2017.09.014.

[5] S.C. Middleburgh, I. Ipatova, L.J. Evitts, M.J.D. Rushton, B. Assinder, R.W. Grimes, W.E. Lee, Evidence of excess oxygen accommodation in yttria partially-stabilized zirconia, Scr. Mater. 175 (2020) 7–10. https://doi.org/10.1016/j.scriptamat.2019.08.040.

[6] D. Pêcheur, J. Godlewski, J. Peybernès, L. Fayette, M. Noé, A. Frichet, O. Kerrec, Contribution to the understanding of the effect of the water chemistry on the oxidation kinetics of Zircaloy-4 cladding, in: ASTM Spec. Tech. Publ., 2000. https://doi.org/10.1520/stp14328s.

[7] O. Roth, J.A. Laverne, Effect of pH on H_2O_2 production in the radiolysis of water, J. Phys. Chem. A. 115 (2011). https://doi.org/10.1021/jp1099927.

[8] W.G. Burns, P.B. Moore, Water radiolysis and its effect upon in reactor zircaloy corrosion, Radiat. Eff. 30 (1976). https://doi.org/10.1080/00337577608240827.

[9] C. Ferradini, J.P. Jay-Gerin, Effect of pH on water radiolysis: a still open question - a minireview, Res. Chem. Intermed. 26 (2000). https://doi.org/10.1163/156856700X00525.

[10] S. Le Caër, Water radiolysis: Influence of oxide surfaces on H_2 production under ionizing radiation, Water (Switzerland). 3 (2011) 235–253. https://doi.org/10.3390/w3010235.

[11] M.C. Song, K.J. Lee, The evaluation of radioactive corrosion product at PWR as change of primary coolant chemistry for long-term fuel cycle, Ann. Nucl. Energy. 30 (2003) 1231–1246. https://doi.org/10.1016/S0306-4549(03)00054-9.

[12] I.D. Dobrevski, K.F. Minkova, R.A. Ivanova, Possible impact on the occurrence of axial offset anomaly, Powr Plant Chem. 5(4) (2018) 197–202.

[13] P.L. Frattini, J. Blok, S. Chauffriat, J. Sawicki, J. Riddle, Axial offset anomaly: Coupling PWR primary chemistry with core design, Nucl. Energy. 40 (2001) 123–135. https://doi.org/10.1680/nuen.40.2.123.39952.

[14] J. Blok, S. Chauffiriat, P. Frattini, Modeling the axial offset anomaly in PWRs, Proc. Int. Conf. Water Chem. Nucl. React. Syst. Optim. New Dev. (2002) 1–9.

[15] J. Mart, A. Klein, A. Soldatov, Feasibility study of a soluble boron-free small modular integral pressurized water reactor, Nucl. Technol. 188 (2014) 8–19. https://doi.org/10.13182/NT13-

135.

[16] B.A. Murgatroyd, J. Winton, Hydriding Zircaloy-2 in lithium hydroxide solutions, J. Nucl. Mater. 23 (1967) 249–256. https://doi.org/10.1016/0022-3115(67)90157-2.

[17] N. Ramasubramanian, Lithium uptake and the corrosion of zirconium alloys in aqueous lithium hydroxide solutions, in: ASTM Spec. Tech. Publ., Publ by ASTM, 1991: pp. 613–626. https://doi.org/10.1520/stp25531s.

[18] D. Pêcheur, J. Godlewski, P. Billot, J. Thomazet, Microstructure of Oxide Films Formed during the Waterside Corrosion of the Zircaloy-4 Cladding in Lithiated Environment, in: Zircon. Nucl. Ind. Elev. Int. Symp., 2009. https://doi.org/10.1520/stp16169s.

[19] N. Ramasubramanian, N. Precoanin, V. Ling, Lithium Uptake and the Accelerated Corrosion of Zirconium Alloys, Zircon. Nucl. Ind. Eighth Int. Symp. (2008) 187-187–15. https://doi.org/10.1520/stp18865s.

[20] J. Eichler, U. Eisele, J. Rödel, Mechanical properties of monoclinic zirconia, J. Am. Ceram. Soc. 87 (2004) 1401–1403. https://doi.org/10.1111/j.1151-2916.2004.tb07748.x.

[21] L. Kurpaska, I. Jozwik, J. Jagielski, Study of sub-oxide phases at the metal-oxide interface in oxidized pure zirconium and Zr-1.0% Nb alloy by using SEM/FIB/EBSD and EDS techniques, J. Nucl. Mater. 476 (2016) 56–62. https://doi.org/10.1016/j.jnucmat.2016.04.038.

[22] W. Qin, C. Nam, H.L. Li, J.A. Szpunar, Effects of local stress on the stability of tetragonal phase in ZrO_2 film, J. Alloys Compd. 437 (2007) 280–284. https://doi.org/10.1016/j.jallcom.2006.07.102.

[23] J. Yang, M. Youssef, B. Yildiz, Electro-chemo-mechanical effects of lithium incorporation in zirconium oxide, Phys. Rev. Mater. 2 (2018). https://doi.org/10.1103/PhysRevMaterials.2.075405.

[24] S.C. Middleburgh, W.E. Lee, M.J.D. Rushton, Structure and properties of amorphous uranium dioxide, Acta Mater. 202 (2021). https://doi.org/10.1016/j.actamat.2020.10.069.

[25] M. Yashima, T. Hirose, S. Katano, Y. Suzuki, M. Kakihana, M. Yoshimura, Structural changes of ZrO_2-CeO_2 solid solutions around the monoclinic-tetragonal phase boundary, Phys. Rev. B. 51 (1995) 8018–8025. https://doi.org/10.1103/PhysRevB.51.8018.

[26] B. Bondars, G. Heidemane, J. Grabis, K. Laschke, H. Boysen, J. Schneider, F. Frey, Powder diffraction investigations of plasma sprayed zirconia, J. Mater. Sci. 30 (1995) 1621–1625. https://doi.org/10.1007/BF00375275.

[27] M. Youssef, B. Yildiz, Intrinsic point-defect equilibria in tetragonal ZrO_2: Density functional theory analysis with finite-temperature effects, Phys. Rev. B - Condens. Matter Mater. Phys. 86 (2012). https://doi.org/10.1103/PhysRevB.86.144109.

[28] U. Guth, Kröger-Vinks Notation of Point Defects, in: Encycl. Appl. Electrochem., 2014. https://doi.org/10.1007/978-1-4419-6996-5_310.

[29] L. Pilote, A.E. Gheribi, P. Chartrand, Study of the solubility of Pb, Bi and Sn in aluminum by mixed CALPHAD/DFT methods: Applicability to aluminum machining alloys, Calphad Comput. Coupling Phase Diagrams Thermochem. 61 (2018) 275–287. https://doi.org/10.1016/j.calphad.2018.04.007.

[30] W.D. Neilson, H. Steele, S.T. Murphy, Evolving Defect Chemistry of $(Pu,Am)O_{2\pm x}$, J. Phys Chem. 28 (2021). https://doi.org/10.1021/acs.jpcc.1c03274.

[31] T. Kido, K. Kanasugi, M. Sugano, K. Komatsu, PWR Zircaloy cladding corrosion behavior: Quantitative analyses, J. Nucl. Mater. 248 (1997) 281–287. https://doi.org/10.1016/S0022-3115(97)00125-6.

[32] Y.R. Than, M.R. Wenman, B.D.C. Bell, S.R. Ortner, H. Swan, R.W. Grimes, Modelling and experimental analysis of the effect of solute iron in thermally grown Zircaloy-4 oxides, J. Nucl. Mater. 509 (2018) 114–123. https://doi.org/10.1016/j.jnucmat.2018.06.029.

[33] K. Johnston, M.R. Castell, A.T. Paxton, M.W. Finnis, $SrTiO_3$(001)(2×1) reconstructions: First-principles calculations of surface energy and atomic structure compared with scanning tunneling microscopy images, Phys. Rev. B - Condens. Matter Mater. Phys. 70 (2004) 1–12. https://doi.org/10.1103/PhysRevB.70.085415.

[34] S. Kasamatsu, T. Tada, S. Watanabe, Theoretical analysis of space charge layer formation at metal/ionic conductor interfaces, Solid State Ionics. 183 (2011) 20–25. https://doi.org/10.1016/j.ssi.2010.11.022.

[35] W.D. Neilson, J.T. Pegg, H. Steele, S.T. Murphy, The defect chemistry of non-stoichiometric $PuO_{2\pm x}$, Phys. Chem. Chem. Phys. 23 (2021) 4544–4554. https://doi.org/10.1039/d0cp06497a.

[36] T.R. Rettich, R. Battino, E. Wilhelm, Solubility of gases in liquids. 22. High-precision determination of Henry's law constants of oxygen in liquid water from T = 274 K to 328 K, J. Chem. Thermodyn. 32 (2000) 1145–1156. https://doi.org/10.1006/jcht.1999.0581.

[37] B.B. Benson, D. Krause, M.A. Peterson, The solubility and isotopic fractionation of gases in dilute aqueous solution. I. Oxygen, J. Solution Chem. 8 (1979) 655–690. https://doi.org/10.1007/BF01033696.

[38] D. Tromans, Temperature and pressure dependent solubility of oxygen in water: A thermodynamic analysis, Hydrometallurgy. 48 (1998) 327–342. https://doi.org/10.1016/s0304-386x(98)00007-3.

[39] J.C. Garcia, L.M.R. Scolfaro, A.T. Lino, V.N. Freire, G.A. Farias, C.C. Silva, H.W.L. Alves, S.C.P. Rodrigues, E.F. Da Silva, Structural, electronic, and optical properties of ZrO_2 from ab initio calculations, J. Appl. Phys. 100 (2006) 1–25. https://doi.org/10.1063/1.2386967.

[40] B.D.C. Bell, S.T. Murphy, P.A. Burr, R.W. Grimes, M.R. Wenman, Accommodation of tin in tetragonal ZrO_2, J. Appl. Phys. 117 (2015). https://doi.org/10.1063/1.4909505.

[41] S.T. Murphy, N.D.M. Hine, Anisotropic charge screening and supercell size convergence of defect formation energies, Phys. Rev. B. 87 (2013) 094111. https://doi.org/10.1103/PhysRevB.87.094111.

[42] S.C. Middleburgh, K.P.D. Lagerlof, R.W. Grimes, Accommodation of excess oxygen in group II monoxides, J. Am. Ceram. Soc. 96 (2013) 308–311. https://doi.org/10.1111/j.1551-2916.2012.05452.x.

[43] M.J.D. Rushton, I. Ipatova, L.J. Evitts, W.E. Lee, S.C. Middleburgh, Stoichiometry deviation in amorphous zirconium dioxide, RSC Adv. 9 (2019) 16320–16327. https://doi.org/10.1039/c9ra01865d.

[44] B.D.C. Bell, S.T. Murphy, P.A. Burr, R.J. Comstock, J.M. Partezana, R.W. Grimes, M.R. Wenman, The influence of alloying elements on the corrosion of Zr alloys, Corros. Sci. 105 (2016) 36–43. https://doi.org/10.1016/j.corsci.2015.12.022.

[45] S. Xie, B. Zhou, X. Liang, Q. Li, W. Liu, M. Yao, J. Zhang, The distribution of Li ions in the oxide film formed on zircaloy-4 corroded in lithiated water at 633 K, Materials (Basel). 13 (2020).

https://doi.org/10.3390/ma13040873.

Supplementary data

Previous publications have utilised the CASTEP DFT when creating Brouwer diagrams. This investigation used CASTEP to confirm Brouwer diagram outputs with VASP DFT.

Table 1. Monoclinic/ defect formation energies computed by VASP and CASTEP at constant volume. Only most stable defect coordinates/cluster arrangements are reported.

Defect	Monoclinic		
	VASP eV	CASTEP eV	Site/Fractional coordinates
$V_O^{\times}$	4.78	5.97	4e (0.5, 0.6, 0.4)
$V_O^{\cdot}$	2.18	3.05	4e (0.5, 0.6, 0.4)
$V_O^{\cdot\cdot}$	0.10	0.16	4e (0.5, 0.6, 0.4)
$V_{Zr}^{\times}$	4.30	6.38	4e (0.4, 0.8, 0.6)
$V_{Zr}^{\prime}$	3.86	5.90	4e (0.4, 0.8, 0.6)
$V_{Zr}^{\prime\prime}$	3.76	5.81	4e (0.4, 0.8, 0.6)
$V_{Zr}^{\prime\prime\prime}$	4.06	5.98	4e (0.4, 0.8, 0.6)
$V_{Zr}^{\prime\prime\prime\prime}$	4.69	6.31	4e (0.4, 0.8, 0.6)
$O_i^{\times}$	0.83	1.67	4e (0.5, 0.5, 0.8)
$O_i^{\prime}$	1.55	3.72	4e (0.5, 0.5, 0.8)
$O_i^{\prime\prime}$	2.95	4.78	4e (0.5, 0.5, 0.8)
$Zr_i^{\times}$	12.56	13.72	4e (0.5, 0.0, 0.2)
$Zr_i^{\cdot}$	9.85	9.93	4e (0.5, 0.0, 0.2)
$Zr_i^{\cdot\cdot}$	7.17	6.53	4e (0.5, 0.0, 0.2)
$Zr_i^{\cdot\cdot\cdot}$	5.24	3.59	4e (0.5, 0.0, 0.2)
$Zr_i^{\cdot\cdot\cdot\cdot}$	3.90	0.97	4e (0.5, 0.0, 0.2)

$Li_i^{\times}$	4.51	5.41	4e (0.5, 0.5, 0.8)
$Li_i^{\cdot}$	0.82	1.74	4e (0.5, 0.5, 0.8)
$Li_{Zr}^{'''}$	8.05	5.58	4e (0.5, 0.5, 0.8)
$Li_{Zr}^{''''}$	12.42	9.39	4e (0.5, 0.5, 0.8)
$\{2Li_i : V_{Zr}\}''$	2.13	6.21	-
$\{2Li_i : V_{Zr}\}'''$	6.20	9.97	-
$\{2Li_i : V_{Zr}\}'''$	10.61	13.96	-
$\{Li_{Zr} : V_O\}'$	4.90	4.55	-

Table 2. Tetragonal defect formation energies computed by VASP and CASTEP at constant volume. Only most stable defect coordinates/cluster arrangements are reported.

Defect	**Tetragonal**		
	VASP eV	**CASTEP eV**	**Site/Fractional coordinates**
$V_O^{\times}$	5.62	5.59	4d (0.6, 0.3, 0.5)
$V_O^{\cdot}$	2.31	2.59	4d (0.6, 0.6, 0.5)
$V_O^{\cdot\cdot}$	-0.84	-0.92	4d (0.6, 0.6, 0.5)
$V_{Zr}^{\times}$	5.20	6.67	2b (0.8, 0.6, 0.4)
$V_{Zr}^{'}$	5.68	6.48	2b (0.8, 0.6, 0.4)
$V_{Zr}^{''}$	6.44	6.46	2b (0.8, 0.6, 0.4)
$V_{Zr}^{'''}$	7.40	6.63	2b (0.8, 0.6, 0.4)
$V_{Zr}^{''''}$	8.61	7.03	2b (0.8, 0.6, 0.4)
$O_i^{\times}$	5.47	3.38	16h (0.6, 0.4, 0.4)
$O_i^{'}$	3.40	4.23	16h (0.6, 0.4, 0.4)
$O_i^{''}$	5.47	5.36	16h (0.6, 0.4, 0.4)
$Zr_i^{\times}$	13.12	13.04	16h (0.8, 0.6, 0.4)
$Zr_i^{\cdot}$	9.90	9.63	16h (0.8, 0.6, 0.4)
$Zr_i^{\cdot\cdot}$	6.86	6.02	16h (0.8, 0.6, 0.4)
$Zr_i^{\cdot\cdot\cdot}$	4.75	3.35	16h (0.8, 0.6, 0.4)
$Zr_i^{\cdot\cdot\cdot\cdot}$	2.65	0.50	16h (0.8, 0.6, 0.4)
$Li_i^{\times}$	6.07	5.89	16h (0.4, 0.4, 0.6)
$Li_i^{\cdot}$	-0.52	4.26	16h (0.4, 0.4, 0.6)
$Li_{Zr}^{'''}$	7.95	5.96	16h (0.4, 0.4, 0.6)
$Li_{Zr}^{''''}$	13.80	10.36	16h (0.4, 0.4, 0.6)
$\{2Li_i : V_{Zr}\}''$	3.02	6.68	-
$\{2Li_i : V_{Zr}\}'''$	8.12	11.03	-

$\{2Li_i : V_{Zr}\}'''$	13.58	15.65	-
$\{Li_{Zr} : V_O\}'$	4.35	3.78	-

The formation energies for the various defects and clusters are detailed in Table 1 for monoclinic ZrO_2 and Table 2 for tetragonal ZrO_2.There is good consistency between the trends and values provided by the VASP and CASTEP simulations.